Exploring Higher-Dimensional Black Holes in Numerical Relativity

Hirotaka YOSHINO[1] and Masaru SHIBATA[2]

[1] *Cosmophysics Group, Institute of Particles and Nuclear Studies, KEK, Tsukuba 305-0801, Japan*
[2] *Yukawa Institute for Theoretical Physics, Kyoto University, Kyoto 606-8502, Japan*

We review the current status of our activity in higher-dimensional numerical relativity. We describe a Baumgarte-Shapiro-Shibata-Nakamura formulation in higher dimensions together with cartoon methods which we employ. We also review numerical results which we derive for two subjects in higher-dimensional numerical relativity: dynamical instability of rapidly rotating Myers-Perry (MP) black holes with one rotational parameter and high-velocity black hole collisions and scatterings. The perspective for the future is briefly described.

§1. Introduction

Numerical relativity is probably the unique approach for exploring dynamical problems in general relativity. In numerical relativity, Einstein's equation,

$$G_{ab} = 8\pi G T_{ab}, \tag{1·1}$$

is numerically solved in the framework of an initial-value formulation of general relativity. In the past decade, the community of numerical relativity achieved significant progress, and now, it is feasible to perform a longterm and accurate simulation for the merger of binary composed of black holes and neutron stars (e.g., Refs. 1)–6) for binary black holes and Ref. 7), 8) for others) and for high-velocity collision of two black holes, that are among the strongest gravitational phenomena in nature.

Higher-dimensional numerical relativity is also being an important issue since the TeV gravity scenarios[9)–12)] and the AdS/CFT correspondence[13)] were proposed. To clarify the nonlinear dynamics in higher-dimensional general relativity, a new implementation in numerical relativity is necessary. Higher-dimensional numerical relativity began in 2003 by a pioneering simulation for a 5-dimensional (5D) black string that is unstable against the Gregory-Laflamme instability.[14),15)] Then, several new formulations have been developed and several simulations have been performed in particular in the last three years.

There are three primary motivations for performing higher-dimensional numerical relativity. The first one is stimulated by the fact that mini black holes may be produced in large accelerators such as Large Hadron Collider (LHC) if the TeV gravity hypotheses are correct. If our 3-dimensional (3D) space is a D_3-brane in large[9),10)] or warped[11)] extra dimensions, the Planck energy could be of O(TeV) and quantum gravity phenomena may emerge in high-energy particle colliders. If the particle energy is larger than the Planck energy in this scenario, mini black holes could be produced[16)–18)] (see also Ref. 19) for a recent review). If a black hole with

mass energy slightly larger than the Planck energy is formed in the LHC, it will subsequently emit the Hawking radiation that may be detected. To accurately predict the rate of the mini black-hole production and its detectability, it is necessary to know the cross section for the black-hole production $\sigma_{\rm BH}$, and the resulting mass and angular momentum of the formed black hole. A lower bound of $\sigma_{\rm BH}$ for the black-hole production was given in Refs. 20) and 21) by numerically solving the apparent horizon at an instance of the collision of Aichelburg-Sexl particles[22] in higher dimensions (see also Ref. 23)). However, the precise value of $\sigma_{\rm BH}$ and the black-hole production rate are necessary for precisely predicting the event rate in the particle collider.

The second motivation is to clarify the fundamental properties of black objects in higher dimensions. 4-dimensional (4D) black holes (Kerr black holes) have been shown to be stable in vacuum irrespective of its mass and spin. By contrast, higher-dimensional black objects are not always stable. For example, the Gregory-Laflamme instability[24] is known for a black string. Also, higher-dimensional rapidly rotating black holes (i.e., the Myers-Perry (MP) black holes[25]) are unstable,[26)–29)] and a black hole on a Randall-Sundrum (RS) brane is also conjectured to be unstable.[30] The condition for the onset of the instabilities and the final fate after their onset are clarified only in numerical relativity (see §3).

The third motivation comes from the hypothesis of the AdS/CFT correspondence, which conjectures that the classical gravity of anti-de Sitter (AdS) spacetime is dual to the conformal field theory (CFT) on the boundary of the AdS spacetime. If this hypothesis holds, we may be able to obtain an idea for phenomena in CFT, for which explicit calculations are difficult due to the strong coupling effect, by studying the dual gravitational system. To calculate time-dependent phenomena in the gravity side which is expected to be dual to the CFT phenomena of interest, numerical relativity will play an important role.

The purpose of this article is to review our activity in higher-dimensional numerical relativity. In §2, we review the Baumgarte-Shapiro-Shibata-Nakamura (BSSN) formulation for higher-dimensional numerical relativity together with the "cartoon methods" for implementing spacetime symmetries, that are employed in our numerical code. In §3, we summarize several test simulations which are useful for validating numerical codes, illustrating that our codes are validated by these test simulations. In §4, we review the simulation results obtained by our group, focusing in particular on the numerical results for rapidly rotating Myers-Perry (MP) black holes that may be dynamically unstable against nonaxisymmetric deformation (§4.1) and high-velocity two-black-hole collisions in a 5D spacetime (§4.2). Section 5 is devoted to a summary and a brief discussion of the issues for the future. Throughout this article, the unit $c = 1$ is used, while the higher-dimensional gravitational constant G is explicitly shown.

§2. Formulation

There are many ingredients necessary for a successful simulation of vacuum spacetimes in numerical relativity: formulations including methods for implementing

spacetime symmetries for a special class of spacetime; appropriate gauge conditions; methods for extracting gravitational waves; techniques for handling black holes; apparent horizon (AH) finder; adaptive mesh refinement (AMR). These ingredients were already developed in 4D numerical relativity. Most of them can be extended for higher-dimensional numerical relativity in a straightforward manner. In this section, we describe the methods of the extension of the BSSN formulation together with the cartoon methods. For a summary of other formulations, we recommend the reader to refer to Ref. 31).

2.1. *BSSN formulation*

In 4D numerical relativity, the BSSN formulation[32),33)] is most popular for a longterm and stable simulation, and its extension for higher-dimensional numerical relativity is straightforward.[34)] The BSSN formulation is in a sense a modified version of the ADM formulation;[35)] the numerical stability is realized by a suitable modification of the ADM formulation. In the following, we briefly review the ADM and the BSSN formulations for D-dimensional spacetimes.

Suppose $\mathcal{M}$ be a D-dimensional spacetime with a metric g_{ab}. Consider a sequence of N-dimensional spacelike hypersurfaces $\Sigma_t(h_{ab}, K_{ab})$ foliated by a time coordinate t in $\mathcal{M}$.*) Here, h_{ab} is the induced metric $h_{ab} := g_{ab} + n_a n_b$ of Σ_t, where n_a is the future-directed unit normal Σ_t, and K_{ab} is the extrinsic curvature defined by $K_{ab} := -(1/2)\pounds_n h_{ab}$, where $\pounds_n$ is the Lie derivative with respect to n^a. The coordinate basis t^a of the time coordinate t is decomposed as $t^a = \alpha n^a + \beta^a$, where α and β^a are the lapse function and the shift vector, respectively. In terms of these variables, the metric is written in the form

$$ds^2 = -\alpha^2 dt^2 + h_{ij}(dx^i + \beta^i dt)(dx^j + \beta^j dt), \tag{2·1}$$

and Einstein's equation in the coordinate basis is rewritten as

$$R + K^2 - K_{ab}K^{ab} = 16\pi G\rho, \tag{2·2}$$

$$D_b K^b{}_a - D_a K = 8\pi G j_a, \tag{2·3}$$

$$\pounds_t h_{ab} = -2\alpha K_{ab} + D_a\beta_b + D_b\beta_a, \tag{2·4}$$

$$\begin{aligned}\pounds_t K_{ab} = &-D_a D_b\alpha + \alpha\left(R^{(\Sigma)}_{ab} - 2K_{ac}K^c{}_b + K_{ab}K\right)\\ &+ \beta^c D_c K_{ab} + K_{bc}D_a\beta^c + K_{ac}D_b\beta^c - 8\pi G\alpha\left[S_{ab} + \frac{\rho - S}{D-2}h_{ab}\right],\end{aligned} \tag{2·5}$$

where Eq. (2·4) is equivalent to the definition of K_{ab}, and Eqs. (2·2), (2·3), and (2·5) are derived from $G_{ab}n^a n^b = 8\pi G\rho$, $G_{bc}n^b h^c{}_a = -8\pi G j_a$, and $G_{cd}h^c{}_a h^d{}_b = 8\pi S_{ab}$ using Gauss, Codazzi, and Ricci equations, respectively. Here, we defined

$$\rho := T_{ab}n^a n^b; \qquad j_a := -T_{bc}n^b h^c{}_a; \qquad S_{ab} := T_{cd}h^c{}_a h^d{}_b, \tag{2·6}$$

*) Latin indices a, b, c, $\cdots$ are the abstract indices, while i, j, k, $\cdots$ denote the components in the coordinate basis.

and $S := S^c{}_c$. $R^{(\Sigma)}_{ab}$ denotes the Ricci tensor with respect to h_{ab}.

Equations (2·2) and (2·3) are Hamiltonian and momentum constraint equations: On the initial spacelike hypersurface (i.e., initial data), these two constraints have to be satisfied. Then, the time evolution of (h_{ij}, K_{ij}) is determined by Eqs. (2·4) and (2·5). The constraint equations are automatically satisfied after the time evolution as long as the evolution equations are solved exactly. However, these constraints are always violated slightly in actual simulations. The violation does not grow with time only in an appropriate formulation, which is necessary in numerical relativity. The BSSN formulation is one of the most popular formulations with which the constraint violation is well controlled.

The basic idea of the BSSN formulation is to increase the number of variables as well as that of constraints to suppress the growth of unphysical modes. Specifically, new variables, χ, $\tilde{h}_{ij}$, $\tilde{A}_{ij}$, and $\tilde{\Gamma}^i$, are defined from

$$\tilde{h}_{ij} = \chi h_{ij}, \quad K_{ij} = \frac{1}{\chi}\left(\tilde{A}_{ij} + \frac{K}{N}\tilde{h}_{ij}\right), \quad \tilde{\Gamma}^i := h^{jk}\tilde{\Gamma}^i_{jk} = -\tilde{h}^{ik}{}_{,k}. \tag{2·7}$$

Here, the conformal factor χ is chosen so that the determinant $\tilde{h}$ of $\tilde{h}_{ij}$ satisfies the condition in the Cartesian coordinates

$$\tilde{h} = 1, \tag{2·8}$$

which is equivalent to setting $\chi = h^{-1/N}$, and $\tilde{\Gamma}^i_{jk}$ denotes the Christoffel symbol with respect to $\tilde{h}_{ij}$. The evolution equations are derived as

$$(\partial_t - \beta^i\partial_i)\chi = \frac{2}{N}\chi\left(\alpha K - \partial_i\beta^i\right), \tag{2·9}$$

$$(\partial_t - \beta^i\partial_i)K = -D_iD^i\alpha + \alpha\left(\tilde{A}^{ij}\tilde{A}_{ij} + \frac{K^2}{N}\right) + \frac{8\pi\alpha}{D-2}\left[(D-3)\rho + S\right], \tag{2·10}$$

$$\begin{aligned}(\partial_t - \beta^j\partial_j)\tilde{\Gamma}^i = {}& -2\tilde{A}^{ij}\partial_j\alpha + 2\alpha\left[\tilde{\Gamma}^i_{jk}\tilde{A}^{jk} - \frac{D-2}{N}\tilde{h}^{ij}K_{,j} - 8\pi\tilde{h}^{ij}j_j - \frac{N\chi_{,j}}{2\chi}\tilde{A}^{ij}\right] \\ & - \tilde{\Gamma}^j\partial_j\beta^i + \frac{2}{N}\tilde{\Gamma}^i\partial_j\beta^j + \frac{D-3}{N}\tilde{h}^{ik}\beta^j_{,jk} + \tilde{h}^{jk}\beta^i_{,jk}.\end{aligned} \tag{2·11}$$

$$(\partial_t - \beta^k\partial_k)\tilde{h}_{ij} = -2\alpha\tilde{A}_{ij} + \tilde{h}_{ik}\partial_j\beta^k + \tilde{h}_{jk}\partial_i\beta^k - \frac{2}{N}\partial_k\beta^k\tilde{h}_{ij}, \tag{2·12}$$

$$\begin{aligned}(\partial_t - \beta^k\partial_k)\tilde{A}_{ij} = {}& \chi\left[-(D_iD_j\alpha)^{\rm TF} + \alpha\left(R^{(\Sigma)\rm TF}_{ij} - 8\pi S^{\rm TF}_{ij}\right)\right] \\ & + \alpha\left(K\tilde{A}_{ij} - 2\tilde{A}_{ik}\tilde{A}^k_j\right) + \tilde{A}_{ik}\partial_j\beta^k + \tilde{A}_{kj}\partial_i\beta^k - \frac{2}{N}\partial_k\beta^k\tilde{A}_{ij},\end{aligned} \tag{2·13}$$

where the indices of $\tilde{A}_{ij}$ are raised and lowered by $\tilde{h}_{ij}$, and TF denotes the trace-free part, e.g., $R^{(\Sigma)\rm TF}_{ij} = R^{(\Sigma)}_{ij} - R^{(\Sigma)}h_{ij}/N$. The Ricci tensor is decomposed into two parts as

$$R^{(\Sigma)}_{ij} = \tilde{R}_{ij} + R^{(\chi)}_{ij}, \tag{2·14}$$

where $\tilde{R}_{ij}$ is the Ricci tensor with respect to $\tilde{h}_{ij}$ and $R^{(\chi)}_{ij}$ is the remaining part composed of the conformal factor, written in the form

$$\tilde{R}_{ij} = -\frac{1}{2}\tilde{h}^{kl}\tilde{h}_{ij,kl} + \frac{1}{2}\left(\tilde{h}_{ki}\partial_j\tilde{\Gamma}^k + \tilde{h}_{kj}\partial_i\tilde{\Gamma}^k\right) - \frac{1}{2}\left(\tilde{h}_{il,k}\tilde{h}^{kl}{}_{,j} + \tilde{h}_{jl,k}\tilde{h}^{kl}{}_{,i} - \tilde{\Gamma}^l\tilde{h}_{ij,l}\right) - \tilde{\Gamma}^l_{ik}\tilde{\Gamma}^k_{jl}, \tag{2·15}$$

$$R^{(\chi)}_{ij} = \frac{(D-3)}{2\chi}\left(\chi_{,ij} - \tilde{\Gamma}^k_{ij}\chi_{,k}\right) - \frac{(D-3)}{4}\frac{\chi_{,i}\chi_{,j}}{\chi^2} + \tilde{h}_{ij}\tilde{h}^{kl}\left[\frac{\chi_{,kl}}{2\chi} - \frac{N\chi_{,k}\chi_{,l}}{4\chi^2}\right] - \frac{1}{2}\tilde{h}_{ij}\frac{\chi_{,m}}{\chi}\tilde{\Gamma}^m. \tag{2·16}$$

The second derivatives of $\tilde{h}_{ij}$ appear only in the first term of Eq. (2·16) (i.e., each component of h_{ij} appears to obey a simple wave equation) and this is the key point for the numerical stability.

In summary, the variables to be evolved are χ, K, $\tilde{h}_{ij}$, $\tilde{A}_{ij}$, and $\tilde{\Gamma}^i$, and they follow Eqs. (2·9), (2·10), (2·12), (2·13), and (2·11), respectively. The conditions $\tilde{A}^i{}_i = 0$, third equation of Eq. (2·7), and Eq. (2·8) are regarded as the new constraints which arise because the number of the dynamical variables are increased. As shown above, the BSSN formulation for higher dimensions has essentially the same form as that for the 4D case, except that some coefficients are changed.

2.2. *Cartoon method*

In the presence of spatial symmetries, it is better to impose such symmetries in numerical simulation to reduce computational costs. In the previous subsection, the BSSN formulation was described assuming that the Cartesian coordinates are used and without assuming the presence of any symmetries a priori. In this subsection, we describe the so-called cartoon method for imposing symmetries in such a formulation.

2.2.1. Cartoon method

The cartoon method was originally proposed by Alcubierre et al.[36] as a prescription for an efficient numerical simulation of axisymmetric 4D spacetimes. The essence in this method is to employ not curvilinear coordinates that possess coordinate singularities, but the Cartesian coordinates. First of all, we briefly review the original idea of the cartoon method.

In an axisymmetric 3D space, the Cartesian coordinates (x, y, z) are introduced so that the z-axis becomes the symmetry axis of axisymmetry ($U(1)$ symmetry) (we refer to this case as "$x = y,\ z$" which indicates that the spatial structures in the x and y directions are equivalent). In the Cartesian coordinates, the $U(1)$ symmetry does not explicitly appear in equations, and we cannot evolve the geometric variables straightforwardly only with the data on, e.g., the (x, z)-plane because y derivatives of them are needed. In the originally cartoon method, a few grid points in the neighborhood of the (x, z)-plane are prepared. Then, the data at a grid point $(x, y \neq 0, z)$ is generated using the data at a point $(\rho, 0, z)$ (i.e., on the (x, z)-plane) where $\rho = \sqrt{x^2 + y^2}$, using the $U(1)$ symmetry. Here, an appropriate interpolation has to be done because the point $(\rho, 0, z)$ is not located on a grid in general. Once the

data at the grid points $y \neq 0$ are known, y derivatives at $y = 0$ are calculated and the data on the (x, z)-plane is evolved toward the next time step. The symmetric relation is $\alpha(x, y, z) = \alpha(\rho, 0, z)$ for a scalar function, and those for vector and tensor functions are also derived by the relations that the Lie derivative of functions with respect to the Killing vector becomes zero.

We described the method for extensions of the cartoon method to 5D spacetimes (4D spaces) in the cases of three types of symmetries, i.e., the $U(1)$ symmetry ("$x,\ y,\ z = w$"), the $U(1) \times U(1)$ symmetry ("$x = y,\ z = w$"), and the $O(3)$ symmetry ("$x = y = z,\ w$") denoting the Cartesian coordinates by (x, y, z, w).[34] For the $U(1)$ symmetry, the extension is straightforwardly done. The cartoon method for the $U(1) \times U(1)$ symmetry is similar to that for the $U(1)$ symmetric case except that two cartoon operations are required in this case. In the case of the $SO(3)$ symmetry, the symmetric relations are different from that for the $U(1)$ symmetric case, but they can be derived in a similar manner (see Ref. 34) for details).

2.2.2. Modified cartoon method

In the original cartoon method, we have to prepare the extra grids in all the symmetric directions. For this reason, as the dimensionality D is increased by 1, the required grid number always increases by a factor of 5 (if we use the 4th-order finite differencing), and thus, a lot of memories are still required for a large value of D. However, this can be avoided by a prescription shown below.[29]

As an example, we here consider an N-dimensional space with the coordinates $(x, y, z, w_1, ..., w_n)$ where $n = D - 4$, and suppose that this space has the $O(D - 3)$ symmetry with respect to $(z, w_1, ..., w_n)$ (i.e., "$z = w_1 = \cdots = w_n$"). The simulation is supposed to be performed on the (x, y, z)-plane. Here, we introduce $\rho = \sqrt{z^2 + \sum_{i=1}^{n} w_i^2}$, and in the following, indices a and b denote x or y. The symmetric relation of a scalar function is

$$\alpha(x, y, z, w_i) = \alpha(x, y, \rho, 0), \tag{2·17}$$

and from this relation, the derivatives are evaluated as

$$\alpha_{,w_i} = \alpha_{,aw_i} = \alpha_{,zw_i} = 0, \qquad \alpha_{,w_i w_j} = (\alpha_{,z}/z)\delta_{ij}. \tag{2·18}$$

The derivatives of vector and tensor functions with respect to w_i can be derived in a similar way using the symmetric relations. Then, all the derivatives necessary for solving the evolution equations can be evaluated without preparing the extra grids. The derivatives with respect to w_i are replaced with those to z or a simple algebraic relation. This implies that additional finite differencing operation is absent. Due to this fact, the computational costs do not increase significantly with this prescription, and the simulation is effectively performed in the $3 + 1$ manner, as in the case that we employ curvilinear coordinates.

§3. Method for code validation

To confirm the reliability of a code newly developed, benchmark tests are necessary. One of the standard tests is to check the convergence of numerical results

with varying grid resolutions: The numerical solution has to show a convergence property that is expected in the employed scheme. Another method is to simulate a spacetime for which an analytic (or semi-analytic) solution is known and to confirm that the numerical results agree with the analytic solution. Here, we summarize the 5D spherically symmetric black hole spacetime in the Gaussian normal coordinates which is useful for the benchmark tests, and show that our code accurately reproduces the solution.

3.1. *Geodesic slice of Schwarzschild-Tangherlini spacetime*

First, we show an analytic solution of the 5D spherical black hole in the geodesic slicing. The well-known metric form of this black hole (the so-called Schwarzschild-Tangherlini metric) is

$$ds^2 = -f(r)dt^2 + \frac{dr^2}{f(r)} + r^2 d\Omega_3^2, \qquad f(r) = 1 - \frac{r_S^2}{r^2}, \tag{3·1}$$

where $d\Omega_3^2$ is the line element of a 3D unit sphere and r_S is the Schwarzschild-Tangherlini radius $r_S = \sqrt{8GM/3\pi}$. Because the coordinates in this metric are not well-behaved inside the event horizon, we rewrite the metric of this spacetime in terms of the Gaussian normal coordinates starting from the $t = 0$ hypersurface as

$$ds^2 = -d\tau^2 + \frac{\left[r_0^2 + (r_S/r_0)^2\tau^2\right]^2}{\left[r_0^2 - (r_S/r_0)^2\tau^2\right]}\frac{dR^2}{R^2} + \left[r_0^2 - (r_S/r_0)^2\,\tau^2\right] d\Omega_3^2, \tag{3·2}$$

where r_0 is defined by

$$r_0 = R\left(1 + \frac{r_S^2}{4R^2}\right). \tag{3·3}$$

The spacetime domain which these coordinates cover is explained as follows. Consider a geodesic congruence of test particles that are initially at rest. Then, each geodesic labels the radial coordinate and its proper time is equal to the time coordinate. At $\tau = 0$, the spatial slice agrees with the Einstein-Rosen bridge written with the isotropic radial coordinate R. This is analogous to the Novikov coordinates in the 4D Schwarzschild spacetime.[37),38)] This line element shows that the RR component of the metric grows and diverges at $\tau = r_0^2/r_S$, at which the slice hits the singularity.

In the line element (3·2), τ and R are always time and radial coordinate, and thus, this coordinate system can be employed in numerical relativity. In this test, a simulation is done with the gauge conditions $\alpha = 1$ and $\beta^i = 0$, until the computation crashes approximately at the crash time $\tau_{\rm crash} = r_S$. Figure 1 shows a comparison between the analytic solution (solid curves) and the data[34)] with grid size $\Delta x/r_S = 0.1$ (crosses, $\times$) and 0.05 (circles, $\odot$). Here, the snapshots of xx component of the conformal 4D metric $\tilde{h}_{xx}$ along the x-axis are drawn for $\tau/r_S = 0.5$, 0.6, 0.7, 0.8, and 0.9. This shows that the numerical solutions agree approximately with the analytic solutions (3·2) (solid curves): The values of $\tilde{h}_{xx}$ rapidly increase and blow up around $x = 1$. It is also checked that the deviation of the numerical solutions from the analytic one shows the 4th-order convergence in a code implementing a 4th-order finite differencing.[34)]

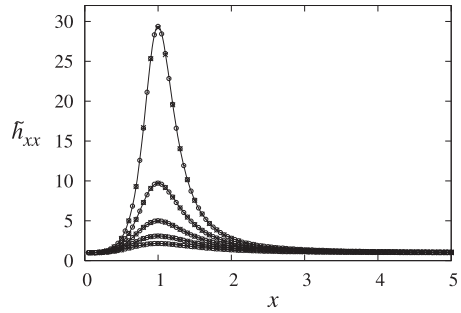

Fig. 1. Snapshots of $\tilde{h}_{xx}$ along the x-axis for $\tau/r_S = 0.5$, 0.6, 0.7, 0.8, and 0.9. The unit of x is $r_S/2$. The grid resolutions are $\Delta x = 0.1$ ($\times$) and 0.05 ($\odot$). The solid curves denote the analytic solutions. The figure is taken from Ref. 34).

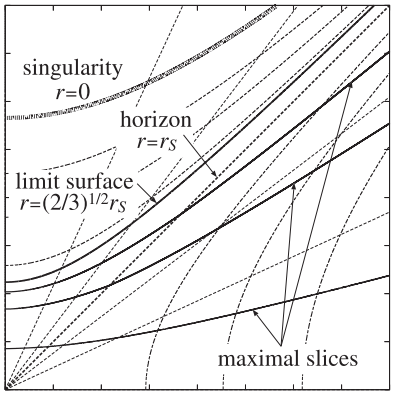

Fig. 2. The sequence of maximal slicing surfaces in the Kruskal diagram of the Schwarzschild-Tangherlini spacetime for $D = 5$. The dotted curves show the $r =$ const. The limit surface is given by $r = \sqrt{2/3} r_S$. The figure is taken from Ref. 41).

3.2. *Limit surface of Schwarzschild-Tangherlini spacetime*

As the second analytic solution, we refer to the limit surface of the maximally sliced evolution (i.e. evolution keeping $K = 0$) of a Schwarzschild-Tangherlini spacetime. In the 4D Schwarzschild black hole, it was shown that the sequence of the maximal slices never hits the curvature singularity but asymptotes to the so-called limit surface,[39] for which an analytical expression of the limit surface, suitable in numerical relativity, was given, e.g., in Ref. 40). The limit surface provides a useful test-bed for calibrating numerical-relativity codes because it is a stationary solution for the black hole. Namely, if we adopt the limit surface as the initial data, the spacelike hypersurface has to be unchanged during the time evolution under certain gauge conditions.

The limit surface for the higher-dimensional black hole is derived by Nakao et al.[41] Figure 2 displays the Kruskal diagram of the 5D Schwarzschild-Tangherlini spacetime. The sequence of maximal-sliced hypersurfaces (starting from the time-symmetric slice) is shown by the solid curves. The sequence asymptotes to $r =$

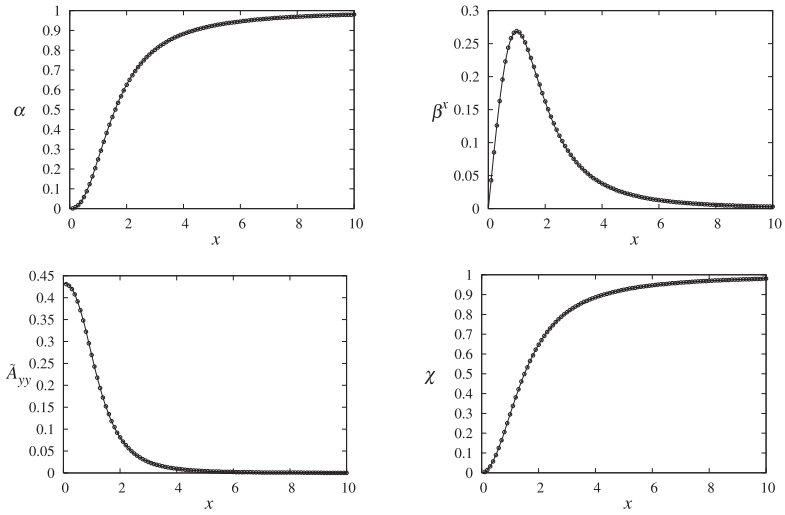

Fig. 3. The analytic solutions of α, β^x, $\tilde{A}_{yy}$, and χ along the x-axis for the limit surface of the 5D spherical black hole (solid curves), and the numerical data after the time evolution at $t = 50r_S$ ($\odot$). Here, the unit of the length is $r_S/2$. The data remains approximately stationary in the time evolution. The figure is taken from Ref. 34).

$\sqrt{2/3}r_S$, which is the limit surface, and the formula for the limit surface can be given analytically also in the 5D case. The limit surface turns out to be conformally flat, and thus, we can introduce the spherical-polar coordinates (R, ϕ_i) in the flat space. The relation between R and the Schwarzschild radial coordinate r is

$$R = \frac{r}{6}\left(3 + \sqrt{3\left[(r_S/r)^2 + 3\right]}\right)\left(\frac{(5+2\sqrt{6})\left[3 - 2(r_S/r)^2\right]}{2(r_S/r)^2 + 15 + 6\sqrt{2\left[(r_S/r)^2+3\right]}}\right)^{1/\sqrt{6}}. \quad (3\cdot4)$$

In terms of the BSSN variables,

$$\chi = \left(\frac{R}{r}\right)^2, \quad \alpha = \sqrt{1 - \left(\frac{r_S}{R}\right)^2\chi + \frac{4}{27}\left(\frac{r_S}{R}\right)^6\chi^3}, \quad (3\cdot5)$$

$$\beta^R = \frac{2}{3\sqrt{3}}\chi^2\left(\frac{r_S}{R}\right)^3, \quad \tilde{A}^R_{\ R} = -3\tilde{A}^{\phi_i}_{\ \ \phi_i} = -\frac{2}{\sqrt{3}}\chi^2\frac{r_S^3}{R^4}. \quad (3\cdot6)$$

Here, r has to be written as a function of R numerically, and then, the nontrivial components can be calculated.

Figure 3 plots the values of α, β^x, $\tilde{A}_{yy}$, and χ along the x-axis at a selected time slice. Adopting the data shown by the solid curves as the initial condition, we evolved this spacetime using the dynamical gauge condition together with Γ-driver.[34] The data at $t = 50r_S$ (after the time evolution) are plotted by the circles. It is confirmed that all the BSSN variables are approximately unchanged in time. In this manner, we can check the reliability of the code using the limit surface solution.

§4. Simulations

In this section, we review our numerical results for two subjects in higher-dimensional numerical relativity: One is on the bar-mode instability of rapidly rotating Myers-Perry (MP) black holes with one rotational parameter[28),29)] and the other is on high-velocity black-hole collisions.[42)]

4.1. *Bar-mode instability of Myers-Perry black holes*

The MP black holes have been inferred to be unstable against certain perturbations.[26),27)] The dynamical instability of rapidly rotating Myers-Perry (MP) black holes with one spin parameter[25)] was explored in Refs. 28), 29) by fully nonlinear simulations, and it was shown that the MP black holes are indeed dynamically unstable if they are rotating sufficiently rapidly, and that the most unstable mode is the bar-mode.[28),29)] In this subsection, we review this study.

4.1.1. The Myers-Perry black holes

In D-dimensional spacetimes, the spacetime can have $\lfloor (D-1)/2 \rfloor$ independent rotational parameters (i.e., the independent components of angular momentum tensor) where $\lfloor x \rfloor$ indicates the largest integer not greater than x. The black hole solutions of spherical horizon topology with arbitrary number of rotational parameters in higher-dimensions were found by Myers and Perry.[25)] Hereafter, we consider only MP black holes with one spin parameter for which the metric is given by[*)]

$$ds^2 = -dt^2 + \frac{\mu}{\Sigma}(dt - a\sin^2\theta d\varphi)^2 + \frac{\Sigma}{\Delta}d\hat{r}^2 + \Sigma d\theta^2 + (\hat{r}^2 + a^2)\sin^2\theta d\varphi^2 + \hat{r}^2\cos^2\theta d\Omega_{D-4}^2, \tag{4·1}$$

where

$$\Sigma = \hat{r}^2 + a^2\cos^2\theta, \qquad \Delta = \hat{r}^2 + a^2 - \mu/\hat{r}^{D-5}. \tag{4·2}$$

In this case, the spacetime has a $U(1)$ symmetry with respect to the rotational plane and an $O(D-4)$ symmetry with respect to the directions orthogonal to the rotational plane. μ and a are related to the mass M and angular momentum J by

$$M = \frac{(D-2)\Omega_{D-2}\mu}{16\pi G}, \qquad J = \frac{2}{(D-2)}Ma. \tag{4·3}$$

The location $\hat{r} = r_K(M, J)$ of the event horizon is given by the equation $\Delta(r_K) = 0$. For $D = 5$, the event horizon exists only for $a < \mu^{1/2}$, whereas it exists for any value of a for $D \geq 6$.

4.1.2. Previous studies

First, we summarize the history for the stability analysis of the MP black hole. A standard method for this is a linear perturbation study. If the variables of the linear perturbation equations are separable, the resulting equation reduces to an ordinary differential equation and its analysis may be done analytically or semi-analytically. Although linear perturbation equations in the MP spacetime have been extensively studied for a metric perturbation, the separation of the variables was succeeded only

[*)] In this section, we use the units of $G = 1 = c$.

for a tensor-mode perturbation.[49),50)] For other modes, the stability has not been found yet by this analysis.

The next best method may be to numerically solve partial differential equations for linear perturbation equations without carrying out the separation of the variables. The first numerical analysis was done by Dias et al.[27)] In this study, an axisymmetric perturbation (i.e., the perturbation that keeps the $U(1) \times O(D-4)$ symmetry) was studied and 2D simultaneous partial differential equations were solved. They discovered that MP black holes with the ultra high spin ($a \gg \mu^{1/(D-3)}$) are unstable against axisymmetric deformation. However, no numerical study has been done for nonaxisymmetric perturbation that breaks the $U(1)$ symmetry.

Alternatively, Emparan and Myers analyzed the stability of MP black holes using two different analysis methods.[26)] In one analysis, they take the so-called black membrane limit of ultra spinning MP black holes. The ultra spinning MP black holes for $D \geq 6$ with $a \gg \mu^{1/(D-3)}$ become extremely oblate. For such an extremely oblate black object, instabilities analogous to the Gregory-Laflamme instability are expected to set in. This discussion was applied to axisymmetric instabilities, and indeed, the numerical analysis of Dias et al. confirms this prediction.[27)]

The other analysis was based on black-hole thermodynamics: They compared the horizon area of a rotating MP black hole with that of two boosted Schwarzschild-Tangherlini black holes, which recede from each other, fixing the total gravitational energy and angular momentum. The horizon area of a MP black hole is

$$A_{\rm MP} = \Omega_{D-2} r_K^{D-2} \left(r_K^2 + a^2\right), \tag{4·4}$$

whereas sum of the area of two boosted black holes is

$$2A_S = 2\Omega_{D-2} r_S(m)^{D-2}, \tag{4·5}$$

where $r_S(m)$ is the horizon radius of a Schwarzschild-Tangherlini black hole. Here, the ADM mass M and the mass m of each black hole are related as $M = 2\sqrt{m^2 + p^2}$ where p is the magnitude of the momentum of each black hole. The angular momentum of the system J is given by $J = bp$, where b is an "impact parameter", i.e., the distance between two black holes in the direction orthogonal to the momenta, chosen to be $b \sim r_S(M)$ as a typical value. If $A_{\rm MP} < 2A_S$, the configuration of two boosted black holes may be preferred to the MP black hole thermodynamically. If this is the case, it is expected that the MP black hole becomes unstable against nonaxisymmetric perturbation, the horizon may pinch off, and the system may change to a state of two boosted black holes. By this discussion, the MP black holes are predicted to be unstable for

$$q := a/\mu^{1/(D-3)} \gtrsim 0.85\ (D=5), \quad 0.96\ (D=6), \quad 0.99\ (D=7), \quad 1.00\ (D=8). \tag{4·6}$$

Here, we introduced a non-dimensional rotational parameter q which is used later. In contrast to the former discussion, this discussion can be applied to $D = 5$ as well as $D \geq 6$, and the predicted critical parameter for the onset of the instability is much smaller than that for the Gregory-Laflamme-like axisymmetric instability (i.e., the instability can set in for a smaller black hole spin). Therefore, the nonaxisymmetric perturbation was predicted to be the primary instability.

4.1.3. Setup of the problem

The prediction by Emparan and Myers seems to be qualitatively correct. However, for strictly verifying that the instability sets in and for quantitatively clarifying the criterion for the onset of the instability, we have to solve Einstein's equation, which can be done only by a numerical-relativity simulation. In the following, we review our latest work.

The simulation was done in the following procedures. First, the MP black hole was written in the quasi-isotropic coordinates in which the radial coordinate is defined by

$$r = r_h \exp\left[\pm \int_{r_K}^{\hat{r}} \frac{d\hat{r}'}{\sqrt{\hat{r}'^2 + a^2 - \mu/\hat{r}'^{(D-5)}}}\right]. \tag{4·7}$$

This is analogous to the isotropic coordinates of the Schwarzschild-Tangherlini spacetime (i.e., the radial coordinate for which the spatial part of the metric becomes conformally flat), and the initial spacelike hypersurface possesses two asymptotically flat regions and one throat (i.e., the structure similar to the Einstein-Rosen bridge). In this quasi-isotropic coordinates, the horizon is located at $r = r_h$. This spacelike hypersurface does not cross the physical curvature singularity of the MP spacetime. Then, the initial data is written in the (x, y, z, w_i) coordinates

$$x = r\cos\theta\cos\phi, \qquad y = r\cos\theta\sin\phi, \qquad \sqrt{z^2 + \sum_i w_i^2} = r\sin\theta, \tag{4·8}$$

where the (x, y)-plane corresponds to the plane of the rotation.

Next, a small nonaxisymmetric perturbation is added to the conformal factor of the BSSN variables, χ, as

$$\chi = \chi_0 \left[1 + A\mu^{-1}(x^2 - y^2)\exp(-r^2/2\hat{r}_K^2)\right], \tag{4·9}$$

where χ_0 is the value of unperturbed initial data, and A is a small number $\ll 1$. This perturbation breaks the $U(1)$ symmetry with respect to (x, y)-plane and keeps the $O(D-4)$ symmetry with respect to z and w_i directions.

Adopting the initial data, we evolved the system by SACRA-ND code, which is a higher-dimensional version of SACRA code.[51] This code employs the 4th-order finite differencing in space and the 4th-order Runge-Kutta method in time with an AMR algorithm. The modified version of the cartoon method explained in §2.2.2 is employed to impose the $O(D-4)$ symmetry. The so-called puncture gauge condition was adopted, and the parameters of the gauge conditions were carefully chosen for stable simulations (see Refs. 28), 29) for details).

4.1.4. Numerical results

The left panel of Fig. 4 shows gravitational waveforms of $m = 2$ mode extracted in a local wave zone as a function of a retarded time for $D = 5$. For $q \lesssim 0.85$, the amplitude exponentially damps with t for $t \geq 8\mu^{1/2}$. This shows that the black hole is stable. By contrast, the amplitude for $q \simeq 0.87$ remains approximately constant, and that for $q \simeq 0.89$ grows exponentially in time. This implies that

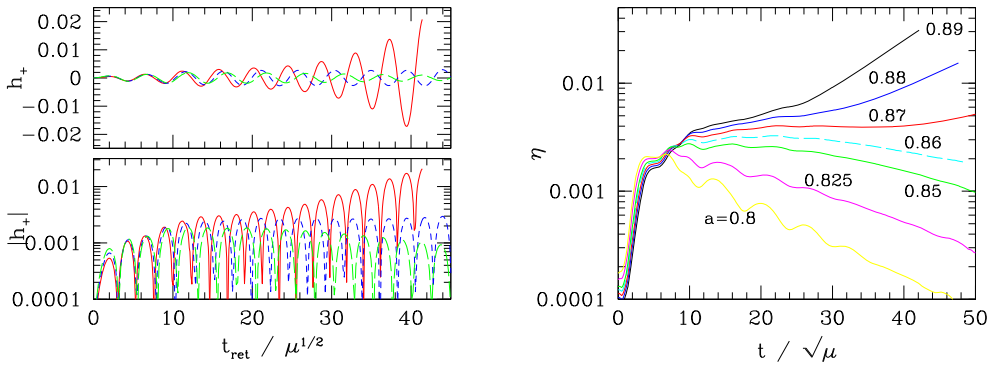

Fig. 4. Left panel: h_+ and its absolute value as functions of retarded time for $a/\mu^{1/2} = 0.85$, 0.87, and 0.89 (dashed, long-dashed, and solid curves) for 5D MP black holes. Right panel: Evolution of distortion parameter η of the apparent horizon for $q = 0.80$–0.89. The figures are taken from Ref. 28).

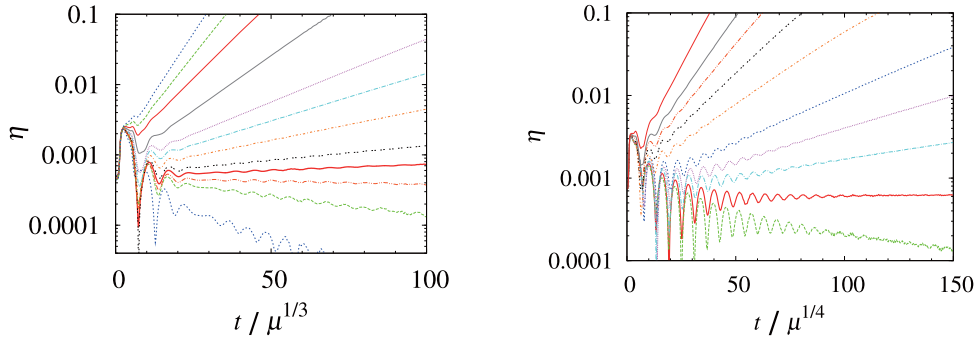

Fig. 5. Left panel: Time evolution of a distortion parameter η for $D = 6$ and for the initial spin $q_i = a/\mu^{1/3} \approx 1.039$, 0.986, 0.933, 0.878, 0.821, 0.801, 0.781, 0.761, 0.750, 0.740, 0.718, and 0.674 (from the upper to lower curves) with $A = 0.005$. Right panel: The same as the left panel but for $D = 7$ and for $q_i = a/\mu^{1/4} = 0.960$, 0.903, 0.844, 0.813, 0.783, 0.767, 0.751, 0.735, and 0.719 (from the upper to lower curves). The figures are taken from Ref. 29).

for $q > 0.87$ the black hole is unstable against nonaxisymmetric deformation. The right panel of Fig. 4 shows the evolution of a distortion parameter η, defined by $\eta := [(l_0 - l_{\pi/2})^2 + (l_{\pi/4} - l_{3\pi/4})^2]^{1/2}/l_0$ where l_φ denotes the proper circumferential length between $\theta = 0$ and $\pi/2$ for a fixed value of φ evaluated on the apparent horizon. This parameter indicates the degree of deviation from the axisymmetry, with $\eta = 0$ for an axisymmetric surface. As the figure shows, the value of η grows exponentially for $q \gtrsim 0.87$, while η damps for $q \lesssim 0.86$. This also shows that the rapidly rotating black hole with $q \gtrsim 0.87$ is unstable against nonaxisymmetric deformation. The critical parameter for the onset of the instability is $q_{\rm crit} \simeq 0.87$.

Figure 5 shows the time evolution of the distortion parameter η for $D = 6$ (left panel) and $D = 7$ (right panel). Here, the definition of η is slightly modified as $\eta := 2[(l_0 - l_{\pi/2})^2 + (l_{\pi/4} - l_{3\pi/4})^2]^{1/2}/(l_0 + l_{\pi/2})$. As in the 5D case, the value of η

Table I. The values of the critical rotational parameter $q_{\rm crit}$ for the onset of the bar-mode instability for $D = 5$–8.

D	5	6	7	8
$q_{\rm crit}$	0.87	0.74	0.73	0.77

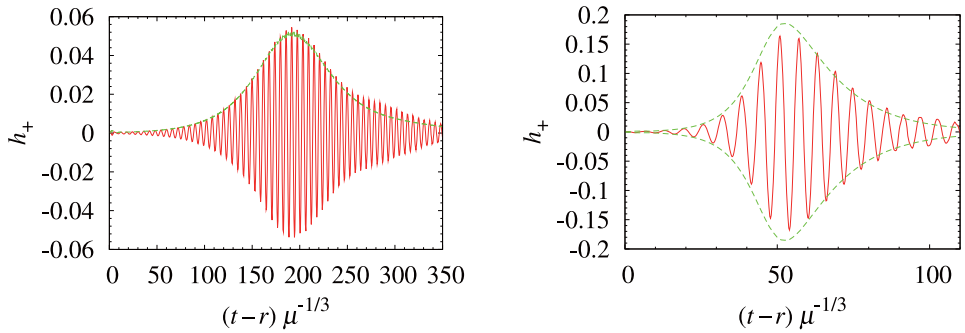

Fig. 6. Left panel: + modes of gravitational waveform (solid curve) emitted from an unstable black hole for $D = 6$ and for $q_i = 0.801$ as a function of a retarded time defined by $t - r$ where r is the coordinate distance from the center. $\eta/2$ is also plotted as a function of t (dashed curve). Right panel: The same as the left panel but for $q_i = 0.986$. The figures are taken from Ref. 29).

exponentially damps in time if q is small, but it grows exponentially for q larger than a certain critical parameter $q_{\rm crit}$. The value of $q_{\rm crit}$ is $\simeq 0.74$ and 0.73 for $D = 6$ and 7, respectively. The critical parameter $q_{\rm crit}$ for the onset of the instability is much smaller than that for the onset of the axisymmetric instability reported in Ref. 27) irrespective of dimensionality D. The results are summarized in Table I.

The solid curves of Fig. 6 plot gravitational waveforms in the longterm simulations where the initial value of q is $q_i = 0.801$ (left panel) and 0.986 (right panel) for $D = 6$. The amplitude of gravitational waves grows in time in the early phase and then saturates when the distortion parameter becomes of order 0.1 at $t = t_{\rm peak}$. After the saturation, the amplitude exponentially damps. The reason is as follows. Associated with the growth of the nonaxisymmetric deformation, emissivity of gravitational waves is enhanced, and energy and angular momentum are significantly extracted from the black hole (although the area increases). As a result, the value of the non-dimensional spin parameter q decreases, and eventually, it becomes $q \simeq q_{\rm crit}$ when the growth of the amplitude saturates at $t = t_{\rm peak}$. Gravitational waves continue to extract energy and angular momentum even after the saturation and the final state is a stable state with the value of $q = q_f$ which is smaller than $q_{\rm crit}$. The time, $t = t_{\rm peak}$, for $q_i = 0.986$ is smaller than that for $q_i = 0.801$. This is because the growth rate of the instability for $q_i = 0.986$ is larger than that for $q_i = 0.801$, and therefore, energy and angular momentum are extracted more efficiently. The dashed curves of Fig. 6 plot half of the distortion parameter η of the apparent horizon. It agrees approximately with the amplitude of gravitational waves, indicating that the distortion of the apparent horizon is not due to a gauge mode and gravitational waves are generated by the distortion of the system.

Figure 7 shows the real part of the gravitational-wave frequency as a function

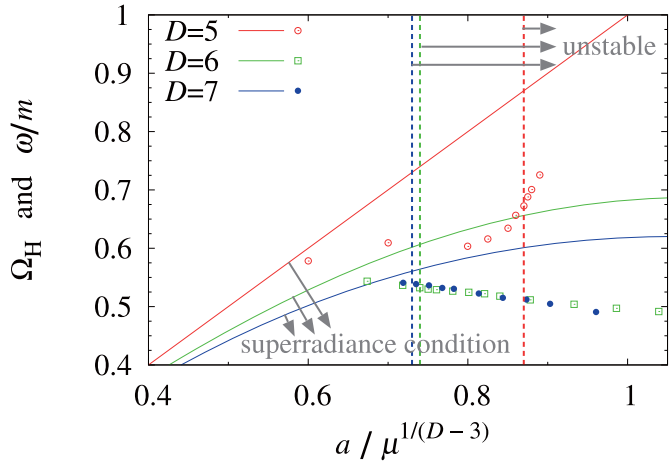

Fig. 7. Real part of gravitational-wave frequencies ω/m (where $m = 2$) for selected values of the spin parameter for $D = 5 - 7$ (points) together with $\Omega_{\rm H}$ as a function of $q = a/\mu^{1/(D-3)}$ for $D = 5 - 7$ (from the upper to lower solid curves). The units of the vertical axis are $\mu^{-1/(D-3)}$. The values $q = q_{\rm crit}$ for the onset of the bar-mode instability are also shown for $D = 5 - 7$ (from the right to left dotted lines). The figure is taken from Ref. 29) with modification.

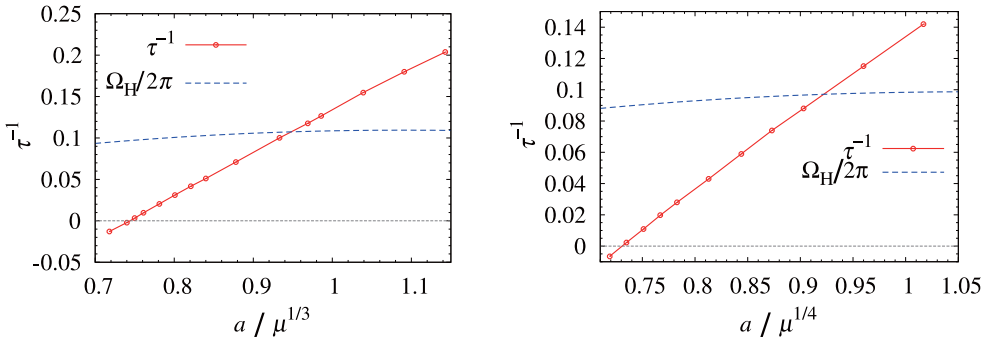

Fig. 8. Left panel: The growth rate $1/\tau$ of η in units of $\mu^{-1/(D-3)}$ as a function of q (solid curve) for $D = 6$. The dashed curve denotes $\Omega_{\rm H}/2\pi$. Right panel: The same as the left panel but for $D = 7$. The figures are taken from Ref. 29).

of q for $D = 5$, 6, and 7. The curve for the superradiance condition[52] $\omega \leq m\Omega_H$ is also shown for each value of D, where $m = 2$ and Ω_H is the angular velocity of the horizon. It is well known that the superradiance condition is the condition such that waves can extract energy and angular momentum from a black hole without violating the area theorem by Hawking. The superradiance condition is a necessary condition for subtracting energy from the black hole by waves. However, it is only a necessary condition and not the sufficient condition for the onset of the dynamical instability found in Refs. 28), 29). In the superradiance often discussed, one considers to inject rather an artificial ingoing wave for which the frequency satisfies this condition. For such an artificial wave, the reflected waves are amplified. For the dynamical instability to occur, gravitational waves have to be spontaneously excited by unstable

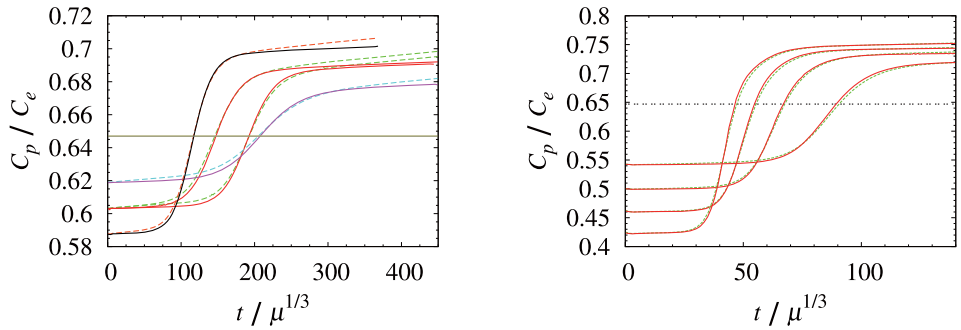

Fig. 9. Left panel: Time evolution of C_p/C_e for $D = 6$ and for non-dimensional spin parameters not much greater than $q_{\rm crit}$, $q_i = a/\mu^{1/3} = 0.821$, 0.801, and 0.781. The corresponding initial values of C_p/C_e are ≈ 0.587, 0.602, and 0.618, respectively. The results with $A = 0.02$ and 0.005 are plotted for $q_i = 0.801$, and the results with $A = 0.02$ are plotted for $q_i = 0.821$ and 0.781. The solid and dashed curves denote the results for high and low resolution runs, respectively. The thin dotted line denote $C_p/C_e = 0.647$ which is the value of C_p/C_e for $q = q_{\rm crit}$. For $q_i = 0.821$, the simulation was stopped at $t/\mu^{1/3} \approx 370$ because the black hole reaches an approximately stationary state. Right panel: The same as the left panel but for the large initial spins $q_i = 0.878$, 0.933, 0.986, and 1.039 with $A = 0.005$. $C_p/C_e \approx 0.542$, 0.499, 0.460, and 0.422 at $t = 0$, respectively. The figures are taken from Ref. 29).

quasinormal modes. Namely, such a mode has to satisfy not only the superradiance condition but also the condition that the imaginary part of the quasinormal mode is negative. Figure 8 shows the inverse τ^{-1} of the growth time scale of the instability for $D = 6$ (left panel) and 7 (right panel), which corresponds to the imaginary part of the quasinormal modes. It indeed becomes negative for $q > q_{\rm crit}$.

The final state eventually reached after the onset of the bar-mode instability for $D = 6$ and 7 was also clarified in Ref. 29). For this purpose, the time evolution of the value of q was approximately followed by evaluating the degree of oblateness of the horizon, C_p/C_e, where $C_p = (l_0 + l_{\pi/2})/2$ and C_e is the proper circumferential length between $\varphi = 0$ and $\pi/2$ along the equatorial plane $\theta = \pi/2$ on the horizon. For a spherically symmetric surface, the value of C_p/C_e is unity, and it monotonically decreases as the spin of the MP black hole increases (as the oblateness of the horizon surface increases). In Ref. 29), the value of C_p/C_e was followed, and using the relation of $C_p/C_e(q)$, the spin, q, is approximately determined.

Figure 9 shows the value of C_p/C_e as a function of time. The value of C_p/C_e increases with time, indicating that the black hole spin decreases. Here, we focus on the curve starting from $C_p/C_e \simeq 0.62$, shown in the left panel. The initial value of q is $q_i = 0.781$, and the value C_p/C_e, which corresponds to $q = q_{\rm crit} = 0.74$, is shown by the dotted line. The curve crosses the dotted line at $t/\mu^{1/3} \simeq 200$, which agrees approximately with the time at which the growth of the gravitational-wave amplitude saturates. The final value of C_p/C_e is $\simeq 0.68$, and the corresponding value of q is $q_f \simeq 0.705$. Thus, a stable and moderately rapidly spinning black hole is the final outcome. Next, we focus on the curve starting from $C_p/C_e \simeq 0.42$ shown in the right panel. In this case, the initial value is $q_i = 1.04$. The value of C_p/C_e increases with time also in this case, and crosses the line for $q = q_{\rm crit}$. Then, it relaxes to a

stable state with the value $C_p/C_e \simeq 0.75$, which corresponds to $q_f = 0.61$. Again, a stable black hole is the final outcome. It is interesting to note that for a high initial spin, the final spin is smaller.

To summarize, the MP black holes are dynamically unstable against nonaxisymmetric bar-mode deformation if they are spinning sufficiently rapidly. As a result of the onset of this instability, energy and angular momentum are extracted from the black hole by gravitational waves which are spontaneously excited by an unstable quasinormal mode.

It should be noted that we could not follow the evolution of the black hole for $q_i \gg 1$. The reason is perhaps that the spatial hypersurface for the large values of q has a very long throat near the event horizon, while the coordinate region to span this throat is limited, and hence, the resolution in space is not sufficient. In this case, the horizon pinch-off might happen as discussed by Emparan and Myers,[26] and it is an interesting remaining issue to clarify the evolution of the instability for this parameter regime.

4.2. *High-velocity collision of black holes in $D = 5$*

The second topic in this section is the high-velocity collision of two black holes for $D = 5$,[42] which is directly related to the mini black hole production at accelerators. The results of a simulation also indicate the possible formation of a naked singularity, and thus, the cosmic censorship hypothesis may not hold in higher dimensions.

4.2.1. Brief history

Here, we briefly summarize the current status for the simulation of high-velocity collision of two black holes. This issue was first explored for $D = 4$: Sperhake et al.[53] performed simulations of the head-on collision of two equal-mass black holes. Subsequently, Shibata, Okawa, and Yamamoto[54] performed simulations of a high-velocity grazing collision of two black holes (i.e., collision with a nonzero impact parameter b) using the SACRA code.[51] Their result indicates that the condition for the black hole merger is approximately $bv/4GE \lesssim 1.25$ for $v \to 1$ (E is the energy of each incoming particle) which is by 50% larger than the condition $b/4GE \lesssim 0.84$ for the apparent horizon formation in the collision of Aichelburg-Sexl particles at the instant of the collision.[21),23)] The radiated energy ΔE and angular momentum ΔJ were evaluated as $\Delta E/M_{\rm ADM} \approx 25 \pm 5\%$ and $\Delta J/J_{\rm ADM} \approx 65 \pm 5\%$, and the resulting black hole near the threshold value of b is a rapidly spinning Kerr black hole with the Kerr parameter $a/M_{\rm BH} \simeq 0.8 \pm 0.1$, where $M_{\rm BH}$ is the mass of the resulting black hole. This result for the high-velocity grazing collision of two black holes was further refined by Sperhake et al.,[55] where they took close attention to the "zoom-whirl" behavior and to the case where a rapidly rotating with $q \sim 0.97$ is formed.

The numerical results for the head-on collision of two black holes in higher-dimensional spacetimes for $D = 5$ were reported in Refs. 44)–46). Because two black holes are initially at rest in their setup, the velocities of the black holes are relatively slow. The first simulation of a high-velocity collision of two black holes for $D = 5$ was reported by Okawa, Nakao, and Shibata.[42] In the following, we review the

results of this simulation.

4.2.2. Setup

To prepare a boosted black hole initial data, the Bowen-York[56] and Brandt-Brügmann[57] formalisms are most popular (see also higher-dimensional generalization[58),59)]). However, the initial data generated by this formalism is known to contain a lot of unphysical radiation. The alternative method, suitable for the high-velocity collision of black holes, was proposed in the 4D case in Ref. 54). Their idea is to first prepare the initial data of one black hole in motion by boosting a Schwarzschild black hole of mass m_0, and then, to superpose those of two boosted black holes. Since there is a nonlinear interaction between two black holes, just superposing the two solutions causes the violation of Hamiltonian and momentum constraints. However, if the initial distance between the two black holes is sufficiently large, violation of the constraints is small, and hence, may be ignored. This method works well also for $D \geq 5$.

Specifically, the method of Refs. 54), 42) is as follows: First, the Schwarzschild-Tangherlini black hole solution in the isotropic coordinates is prepared:

$$ds^2 = -\alpha^2(\bar{r})d\bar{t}^2 + \psi^2(\bar{r})(d\bar{w}^2 + d\bar{x}^2 + d\bar{y}^2 + d\bar{z}^2), \tag{4·10}$$

where

$$\psi(\bar{r}) = 1 + \left(\frac{r_S(m_0)}{2\bar{r}}\right)^2 \qquad \text{and} \qquad \alpha(\bar{r}) = \frac{2 - \psi(\bar{r})}{\psi(\bar{r})}. \tag{4·11}$$

For this seed metric, the Lorentz transformation

$$t = \gamma(\bar{t} \mp v\bar{w}), \qquad w = \gamma(\mp v\bar{t} + \bar{w}), \qquad x = \bar{x}, \qquad y = \bar{y} \tag{4·12}$$

and then, the spatial translations $w \to w \mp d/2$ and $x \to x \mp b/2$ are performed. Note that d is the coordinate separation along the w direction and b the impact parameter of the two black holes. Then, we have the two metrics

$$ds_\pm^2 = -\gamma^2(\alpha_\pm^2 - v^2\psi_\pm^2)dt^2 \pm 2\gamma^2 v(\alpha_\pm^2 - \psi_\pm^2)dtdw + \psi_\pm^2(B_\pm^2 dw^2 + dx^2 + dy^2 + dz^2), \tag{4·13}$$

with $\alpha_\pm = \alpha(\bar{r}_\pm)$, $\psi_\pm = \psi(\bar{r}_\pm)$, and $B_\pm^2 = \gamma^2(1 - v^2\alpha_\pm^2/\psi_\pm^2)$ with

$$\bar{r}_\pm = \sqrt{\gamma^2(w \mp d/2 \pm vt)^2 + (x \mp b/2)^2 + y^2 + z^2}. \tag{4·14}$$

Equation (4·13) describes the black holes ($\pm$) located at $(w, x, y, z) = (\pm d/2, \pm b/2, 0, 0)$ with the velocity $\boldsymbol{v} = (\mp v, 0, 0, 0)$. From these metrics, the extrinsic curvature $K_{ij}^\pm$ can be determined for the black holes ($\pm$). Then, the extrinsic curvature for the initial data of the two-black-hole system is set to be

$$K_{ij} = K_{ij}^+ + K_{ij}^- + \delta K_{ij}, \tag{4·15}$$

where δK_{ij} is a correction due to the mutual nonlinear interaction between the two black holes. Because it is sufficiently small for a large value of $d \gg r_S(m_0)$, it may be approximated as $\delta K_{ij} = 0$ as far as the truncation error is larger than it. The initial spatial metric h_{ij} is written in the form

$$h_{ij}dx^i dx^j = (\Psi + \delta\Psi)^2(B^2 dw^2 + dx^2 + dy^2 + dz^2), \tag{4·16}$$

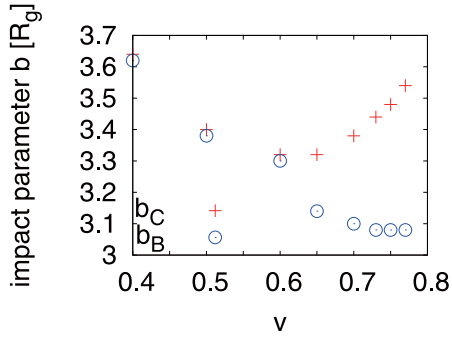

Fig. 10. The values of the impact parameters b_B and b_C, for which black holes are confirmed to merge to a single black hole (for $b \leq b_B$) and to be scattered away (for $b \leq b_C$), as functions of the initial velocity v. The figure is taken from Ref. 42).

where

$$\Psi = \psi_+(\bar{r}_+) + \psi_-(\bar{r}_-) - 1 \qquad \text{and} \qquad B^2 = \gamma^2 \left[1 - \frac{v^2}{\Psi^4}(2-\Psi)^2\right]. \tag{4·17}$$

Here, $\delta\Psi$ is a correction due to the mutual nonlinear interaction and it is also set to be zero for a choice $d \gg r_S(m_0)$.

4.2.3. Numerical results

Adopting the initial data described in the previous subsection, numerical simulations were performed using SACRA-ND code with the moving puncture gauge condition. In contrast to the 4D case, the collision process is simply divided into two cases: two black holes merge at the instance of the first collision; or after the first contact, they scatter away to infinity. Figure 10 shows the values of b_B and b_C as functions of v. Here, the implications for b_B and b_C are as follows: For $b \leq b_B$, the numerical simulation confirms that two black holes merge to be a single black hole and for $b \geq b_C$, two black holes go away to infinity after the scattering. For $v \leq 0.6$, the values of b_B and b_C are identical, implying that the simulations are successfully performed for any value of the impact parameter to determine the final fate. By contrast, for $v \geq 0.65$, b_B and b_C are different, because for $b_B < b < b_C$, the simulation crashes soon after the collision: The largest value of b for the black hole formation would be between b_B and b_C, but the simulations were not able to determine the threshold value.

Then, the authors focused attention to the behavior of a curvature invariant $\mathcal{K} := (6\sqrt{2}E_P^2)^{-1}|R^{abcd}R_{abcd}|^{1/2}$ in the scattering process for $b(> b_C) \to b_C$. Here, E_P is the Planck energy $E_P := \sqrt{3\pi/8G}$ and the normalization factor $(6\sqrt{2}E_P^2)$ of $\mathcal{K}$ is adopted as the value of $|R^{abcd}R_{abcd}|^{1/2}$ at the horizon of a black hole with mass E_P. Figure 11 displays the maps of $\mathcal{K}$ for various stages (before collision, at the instant of collision, after collision from left to right) in the scattering process of two black holes for $v = 0.7$ and $b = 3.38R_g$. At the instant of the collision, the curvature invariant $\mathcal{K}$ steeply increases around the center of mass, and it subsequently decreases with increasing the separation of two black holes after the scattering. The maximum value

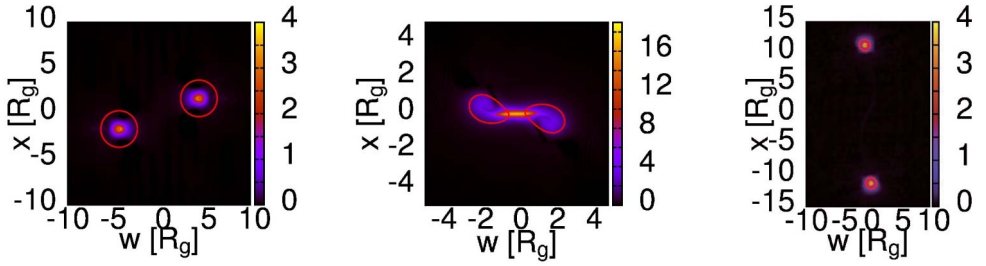

Fig. 11. Maps of $\mathcal{K}$ in the scattering of two black holes with $v = 0.7$ and $b = 3.38R_g$ before scattering (left), at the instant of the collision (middle), and after scattering (right). Here, R_g is the gravitational radius of each incoming black hole $R_g = r_S(m_0)$ (therefore the gravitational radius of the system is $r_S(2E) = \sqrt{2\gamma}R_g$). The figure is taken from Ref. 42).

$\mathcal{K}_{\max}$ of $\mathcal{K}$ is estimated to be

$$\mathcal{K}_{\max} \simeq 50 \left(\frac{E_P}{2E} \right), \tag{4·18}$$

where $E = \gamma m_0$ is the energy of each incoming particle. For the scattering of two black holes with energy $E \simeq (\text{few})E_P$, the value of $\mathcal{K}$ becomes $O(10)$. Furthermore, the value of $\mathcal{K}_{\max}$ steeply increases with decreasing the value of b toward b_C. This suggests that a region outside the horizons, where the curvature is so large that the effect of quantum gravity may play an important role, could appear in the trans-Planckian scattering.

If this happens, the hypothetical mini-black-hole phenomena at accelerators frequently discussed may have to be changed: The black hole production rate becomes smaller and instead we may observe more phenomena of quantum gravity. Unfortunately, the simulations have not provided a totally reliable evidence for/against the naked singularity formation. Obviously, further analyses for $b_B < b < b_C$ with $v \geq 0.65$ are necessary in the future.

§5. Summary

In this article, we reviewed the current status of our activity in higher-dimensional numerical relativity. As described in §2, the formulation necessary for stable simulations of higher-dimensional spacetimes has been established, and the reliable numerical codes have been implemented as shown in §3. In §4, we reviewed two subjects which have been explored by our codes; the fully numerical analysis of the dynamical instability of rapidly rotating MP black holes and the high-velocity collision of two black holes. We expect that a wide variety of extensions will be possible in the near future. For example, the simulation of unstable black objects such as black rings[60] is an interesting subject. The Gregory-Laflamme instability of a Kerr string and the dependence of the fate of the instability on the dimensionality D are also interesting. Among others, the refinement of the simulation of the high-velocity black hole collision seems to be a very important remaining issue to clarify the possible phenomena of mini black hole and quantum gravity in LHC.

In §1, we introduced AdS/CFT correspondence as one of the subjects for higher-dimensional numerical relativity. To study the issues of AdS/CFT correspondence in numerical relativity, a formulation to handle the spacetimes with a negative cosmological constant $\Lambda < 0$ has to be developed. The formulation for handling $\Lambda < 0$ is also necessary for simulating black hole dynamics in the Randall-Sundrum braneworld scenarios.

Another interesting direction in the future is to develop formulations and codes for simulating spacetimes in Gauss-Bonnet gravity[62] (or, more generally, Lovelock gravity[63]). The Gauss-Bonnet gravity is a theory derived from a Lagrangian density with higher-order curvature terms, $\mathcal{L} = R + \alpha_{\rm GB}\mathcal{L}_{\rm GB}$ and $\mathcal{L}_{\rm GB} = R^2 - 4R_{MN}R^{MN} + R_{KLMN}R^{KLMN}$, but is a well-behaved theory in the sense that the 3rd and 4th-order derivative terms of the metric do not appear in equations. The presence of the Gauss-Bonnet terms is predicted by low-energy limit of heterotic string theory. Because the higher-curvature terms may become important in mini black hole production at accelerators and it causes a lot of interesting phenomena such as instabilities of spherically symmetric black holes,[64] exploring the dynamics of the higher-curvature theory will be an interesting subject. The $(N+1)$-formalism for Gauss-Bonnet gravity, which corresponds to the ADM formalism in general relativity, was developed by Torii and Shinkai,[65] and the first numerical study for the black hole initial data in Gauss-Bonnet gravity was done by Yoshino.[66] Further development in this field is expected.

References

1) F. Pretorius, Phys. Rev. Lett. **95** (2005), 121101.
2) M. Campanelli, C. O. Lousto, P. Marronetti and Y. Zlochower, Phys. Rev. Lett. **96** (2006), 111101.
3) J. G. Baker, J. Centrella, D. I. Choi, M. Koppitz and J. van Meter, Phys. Rev. Lett. **96** (2006), 111102.
4) P. Diener et al., Phys. Rev. Lett. **96** (2006), 121101.
5) F. Herrmann, I. Hinder, D. Shoemaker and P. Laguna, gr-qc/0601026.
6) M. Boyle, D. A. Brown, L. E. Kidder, A. H. Mroue, H. P. Pfeiffer, M. A. Scheel, G. B. Cook, and S. A. Teukolsky, Phys. Rev. D **76** (2007), 124038.
7) M. D. Duez, Class. Quant. Grav. **27** (2010), 114002.
8) M. Shibata and K. Taniguchi, Living Rev. Rel. (2011), to appear.
9) N. Arkani-Hamed, S. Dimopoulos and G. R. Dvali, Phys. Lett. B **429** (1998), 263.
10) I. Antoniadis, N. Arkani-Hamed, S. Dimopoulos and G. R. Dvali, Phys. Lett. B **436** (1998), 257.
11) L. Randall and R. Sundrum, Phys. Rev. Lett. **83** (1999), 3370.
12) L. Randall and R. Sundrum, Phys. Rev. Lett. **83** (1999), 4690.
13) J. M. Maldacena, Adv. Theor. Math. Phys. **2** (1998), 231; Int. J. Theor. Phys. **38** (1999), 1113.
14) M. Choptuik, L. Lehner, I. I. Olabarrieta, R. Petryk, F. Pretorius and H. Villegas, Phys. Rev. D **68** (2003), 044001.
15) D. Garfinkle, L. Lehner and F. Pretorius, Phys. Rev. D **71** (2005), 064009.
16) T. Banks and W. Fischler, hep-th/9906038.
17) S. Dimopoulos and G. Landsberg, Phys. Rev. Lett. **87** (2001), 161602.
18) S. B. Giddings and S. Thomas, Phys. Rev. D **65** (2002), 056010.
19) P. Kanti, Lect. Notes Phys. **769** (2009), 387.
20) H. Yoshino and Y. Nambu, Phys. Rev. D **67** (2003), 024009.
21) H. Yoshino and V. S. Rychkov, Phys. Rev. D **71** (2005), 104028.
22) P. C. Aichelburg and R. U. Sexl, Gen. Relat. Gravit. **2** (1971), 303.

23) D. M. Eardley and S. B. Giddings, Phys. Rev. D **66** (2002), 044011.
24) R. Gregory and R. Laflamme, Phys. Rev. Lett. **70** (1993), 2837.
25) R. C. Myers and M. J. Perry, Ann. of Phys. **172** (1986), 304.
26) R. Emparan and R. C. Myers, J. High Energy Phys. **09** (2003), 025.
27) O. J. C. Dias, P. Figueras, R. Monteiro, J. E. Santos and R. Emparan, Phys. Rev. D **80** (2009), 111701.
28) M. Shibata and H. Yoshino, Phys. Rev. D **81** (2010), 021501.
29) M. Shibata and H. Yoshino, Phys. Rev. D **81** (2010), 104035.
30) H. Yoshino, J. High Energy Phys. **01** (2009), 068.
31) H. Yoshino and M. Shibata, Prog. Theor. Phys. Suppl. No. 189 (2011), 269.
32) M. Shibata and T. Nakamura, Phys. Rev. D **52** (1995), 5428.
33) T. W. Baumgarte and S. L. Shapiro, Phys. Rev. D **59** (1998), 024007.
34) H. Yoshino and M. Shibata, Phys. Rev. D **80** (2009), 084025.
35) R. Arnowitt, S. Deser and C. W. Misner, in *Gravitation: An Introduction to Current Research*, ed. L. Witten (Wiley, 1962), p. 227.
36) M. Alcubierre, S. Brandt, B. Brügmann, D. Holz, E. Seidel, R. Takahashi and J. Thornburg, Int. J. Mod. Phys. D **10** (2001), 273.
37) I. Novikov, Ph.D. thesis (Shternberg Astronomical Institute, Moscow, 1963).
38) C. Misner, K. Thorne, and J. Wheeler, *Gravitation* (W. H. Freeman and Company, San Francisco, 1973), p. 826.
39) F. Estabrook, H. Wahlquist, S. Christensen, B. DeWitt, L. Smarr and E. Tsiang, Phys. Rev. D **7** (1973), 2814.
40) T. W. Baumgarte and S. G. Naculich, Phys. Rev. D **75** (2007), 067502.
41) K. I. Nakao, H. Abe, H. Yoshino and M. Shibata, Phys. Rev. D **80** (2009), 084028.
42) H. Okawa, K. i. Nakao, and M. Shibata, arXiv:1105.3331.
43) L. Lehner and F. Pretorius, Phys. Rev. Lett. **105** (2010), 101102.
44) M. Zilhao, H. Witek, U. Sperhake, V. Cardoso, L. Gualtieri, C. Herdeiro and A. Nerozzi, Phys. Rev. D **81** (2010), 084052.
45) H. Witek, M. Zilhao, L. Gualtieri, V. Cardoso, C. Herdeiro, A. Nerozzi and U. Sperhake, Phys. Rev. D **82** (2010), 104014.
46) H. Witek, V. Cardoso, L. Gualtieri, C. Herdeiro, U. Sperhake and M. Zilhao, Phys. Rev. D **83** (2011), 044017.
47) E. Sorkin, Phys. Rev. D **81** (2010), 084062.
48) Y. Yamada and H. Shinkai, Phys. Rev. D **83** (2011), 064006, arXiv:1102.2090.
49) T. Oota and Y. Yasui, Int. J. Mod. Phys. A **25** (2010), 3055.
50) H. Kodama, R. A. Konoplya and A. Zhidenko, Phys. Rev. D **81** (2010), 044007.
51) T. Yamamoto, M. Shibata and K. Taniguchi, Phys. Rev. D **78** (2008), 064054.
52) S. A. Teukolsky and W. H. Press, Astrophys. J. **193** (1974), 443.
53) U. Sperhake, V. Cardoso, F. Pretorius, E. Berti and J. A. González, Phys. Rev. Lett. **101** (2008), 161101.
54) M. Shibata, H. Okawa and T. Yamamoto, Phys. Rev. D **78** (2008), 101501(R).
55) U. Sperhake, V. Cardoso, F. Pretorius, E. Berti, T. Hinderer and N. Yunes, Phys. Rev. Lett. **103** (2009), 131102.
56) J. M. Bowen and J. W. York, Jr., Phys. Rev. D **21** (1980), 2047.
57) S. Brandt and B. Brugmann, Phys. Rev. Lett. **78** (1997), 3606.
58) H. Yoshino, T. Shiromizu and M. Shibata, Phys. Rev. D **72** (2005), 084020.
59) H. Yoshino, T. Shiromizu and M. Shibata, Phys. Rev. D **74** (2006), 124022.
60) R. Emparan and H. S. Reall, Phys. Rev. Lett. **88** (2002), 101101.
61) H. Witek, V. Cardoso, C. Herdeiro, A. Nerozzi, U. Sperhake and M. Zilhao, Phys. Rev. D **82** (2010), 104037.
62) C. Lanczos, Ann. Math. **39** (1938), 842.
63) D. Lovelock, J. Math. Phys. **12** (1971), 498.
64) M. Beroiz, G. Dotti and R. J. Gleiser, Phys. Rev. D **76** (2007), 024012.
65) T. Torii and H. Shinkai, Phys. Rev. D **78** (2008), 084037.
66) H. Yoshino, Phys. Rev. D **83** (2011), 104010.